TU Delft

Delft University of Technology

Mode I fracture behavior of glass fiber composite-steel bonded interface Experiments and CZM

He, Pei; Moreira Arouche, Marcio; Koetsier, Mathieu; Pavlovic, Marko

DOI
10.1016/j.compstruct.2023.117814

Publication date
2024

Document Version
Final published version

Published in
Composite Structures

Citation (APA)
He, P., Moreira Arouche, M., Koetsier, M., & Pavlovic, M. (2024). Mode I fracture behavior of glass fiber composite-steel bonded interface: Experiments and CZM. *Composite Structures*, *330*, Article 117814. https://doi.org/10.1016/j.compstruct.2023.117814

Important note
To cite this publication, please use the final published version (if applicable).
Please check the document version above.

Copyright
Other than for strictly personal use, it is not permitted to download, forward or distribute the text or part of it, without the consent of the author(s) and/or copyright holder(s), unless the work is under an open content license such as Creative Commons.

Takedown policy
Please contact us and provide details if you believe this document breaches copyrights.
We will remove access to the work immediately and investigate your claim.

This work is downloaded from Delft University of Technology.
For technical reasons the number of authors shown on this cover page is limited to a maximum of 10.

Composite Structures 330 (2024) 117814

Contents lists available at ScienceDirect

Composite Structures

journal homepage: www.elsevier.com/locate/compstruct

Mode I fracture behavior of glass fiber composite-steel bonded interface – Experiments and CZM

Pei He [a], Marcio Moreira Arouche [a], Mathieu Koetsier [a], Marko Pavlovic [a,*]

[a] *Faculty of Civil Engineering and Geosciences, Delft University of Technology, Netherlands*

ARTICLE INFO

Keywords:
Composite-steel bonded interface
mode I fracture behavior
DCB
DIC
Four-linear traction-separation law
CZM

ABSTRACT

Debonding is characterized as the governing failure mode in the innovative wrapped composite joints made with glass fiber composite material wrapped around steel hollow sections without welding. The prerequisite for predicting debonding failure of wrapped composite joints is to obtain fracture behavior of the composite-steel bonded interface. The mode I fracture behavior of the bonded interface was experimentally investigated using glass fiber composite-steel double cantilever beam (DCB) specimens. The crack length a and the crack tip opening displacement (CTOD) during the test were accurately measured by analyzing the digital image correlation (DIC) data while the strain energy release rate (SERR) was calculated through the extended global method (EGM). The cohesive zone modeling (CZM) was utilized in the finite element model with the proposal of a four-linear traction-separation law to simulate the mode I fracture process. An approach is introduced to determine the critical stages of the proposed four-linear cohesive law by combining accurate measurements of crack length a and CTOD, along with SERR values. The validity of the four-linear cohesive law and the introduced approach to determine the critical stages were confirmed by good agreement in both global and local behavior between the testing and the FEA results.

1. Introduction

To fully unlock application potential of CHS (circular hollow sections) restricted by current welding technology in many cases, the concept of non-welded wrapped composite joints was proposed by TU Delft [1] as an alternative to traditional welded joints, as shown in Fig. 1a). CHS brace members (diagonals) and the chord member in this case are bonded together by composite wrap which can be shaped in an optimal manner to decrease stress concentration at the bonded interface. The initial tensile static tests proved improved initial stiffness and equivalent load resistance of wrapped composite joints compared to welded joints [2–4] while the subsequent fatigue experiments validated their lower stiffness degradation and superior fatigue life than the welded joints [5,6]. It was found that debonding of the composite-steel bonded interface is the predominant failure mode of wrapped composite joints subjected to axial load [3,4], as shown in Fig. 1b). It is therefore imperative to understand the fracture behavior of the composite-steel bonded interface as a prerequisite for prediction of the joint resistance. An interfacial crack can propagate in three different fracture modes in fracture mechanics: mode I (opening), mode II (in-plane shear) and mode III (out-of-plane shear), as illustrated in Fig. 2. Although mode II failure governs at the root of the primary bonded interface attributed to dominance of through thickness shear stresses, mode I failure is pronounced at the secondary bonded interface due to local bending of the composite wrap and at the end of the primary bonded interface attributed to contraction of the brace cross section resulting from steel yielding [3], see Fig. 1b).

The double cantilever beam (DCB) specimen configuration was initially used in the standard [7,8] for evaluation of delamination in unidirectional composites under mode I loading, and was utilized by many researchers to acquire fracture properties of the adhesively bonded joints [9–12]. It should be noted that all the experimental and numerical work mentioned above were based on the symmetric DCB (same material and same thickness) configurations. Recently some researchers [13–18] also investigated the fracture behavior of the asymmetric composite-metal DCB specimen which was more complex due to the following three reasons:

a) the inherently existed mode mixity as a result of loading asymmetry and material asymmetry across the interface [19];

* Corresponding author.
E-mail address: M.Pavlovic@tudelft.nl (M. Pavlovic).

https://doi.org/10.1016/j.compstruct.2023.117814
Received 10 July 2023; Received in revised form 16 September 2023; Accepted 13 December 2023
Available online 15 December 2023
0263-8223/© 2023 The Authors. Published by Elsevier Ltd. This is an open access article under the CC BY license (http://creativecommons.org/licenses/by/4.0/).

b) dependency of interfacial fracture behavior on the material and surface treatment of the adherends, types of resin and adhesive;
c) the range of the fracture toughness is related to the crack growth location within the bondline which is affected by the degree of the stiffness mismatch between the adhesive layer and the adherends [20].
d) non-linear behavior of the interface attributed to large deformation of metal adherend where LEFM may not work.

To remove the mode mixity attributed to the in-plane sliding, the design of bi-material DCB configuration based on the criterion that the two arms have the same longitudinal strain distribution at the faying surfaces was proposed and validated in some research studies [16,17,21,22].

The strain energy release rate (SERR) evaluation is pursued to acquire the fracture resistance for crack initiation and crack propagation, and to obtain the R-curve behavior. Normally, the SERR can be calculated by the conventional compliance calibration (CCM) method where the function between the specimen compliance and the crack length can be derived experimentally [7,8]. But it requires continuous and accurate measurements of crack length during testing which are not easy to obtain and may lead to important errors during the characterization [23]. On the other hand, it was found that CCM cannot be used for the mode partitioning of mixed-mode results as in the case for the asymmetric and layered joint configuration [24]. An alternative called the extended global method (EGM) based on the beam theory [25] was used for SERR calculation and mode partitioning in bi-material DCB tests [18,24,26,27]. In those tests the crack tip was observed visually by marked vertical lines or cameras which is not accurate and may be not suitable in the case of negligible adhesive layer. On the other hand, the crack tip opening displacement (CTOD) cannot be measured.

In the fracture problems of the composite-metal interface, LEFM cannot be used for fracture analysis. The reason is that the plastic strain in the steel adherend and in the ductile adhesive contribute to the strain energy, thereby hampering correct assessment of fracture toughness of the interface [28,29]. Additionally, existence of fiber bridging hinders the crack growth, resulting in a non-linear fracture process zone (FPZ) forming in the wake of the crack tip, the size of which is negligible [30–32]. The non-linear FPZ can be approximately in conjunction with computational techniques by utilizing the cohesive zone modeling (CZM) [33,34] where the constitutive behavior of the FPZ is defined by the traction-separation law derived from laboratory tests. The shape of the cohesive law is highly dependent on the material properties, composite layup, adherend surface treatment, etc. The CZM has been extensively applied in the numerical simulation of delamination in composites [24,27,35–38]. Unluckily, there is limited research studies in terms of applying cohesive zone model in simulation of composite-steel bonded interface [39].

This paper focused on the acquisition of mode I fracture behavior of glass fiber composite-steel bonded interface used in the non-welded wrapped composite joints by DCB test and DCB modeling. 2D DIC technique was used to accurately measure the crack length and the crack tip opening displacement during the tests while The SERR was calculated by EGM. A four-linear traction-separation law was proposed in the CZM to simulate the mode I failure process in the FE model. An approach was introduced that combines accurate measurements of crack length and CTOD, along with SERR values, to determine the characteristic stages within the four-linear cohesive law. To validate both the four-linear cohesive law and the approach for determining its critical stages, a comparison was made in term of the global and local behavior between experimental and numerical results.

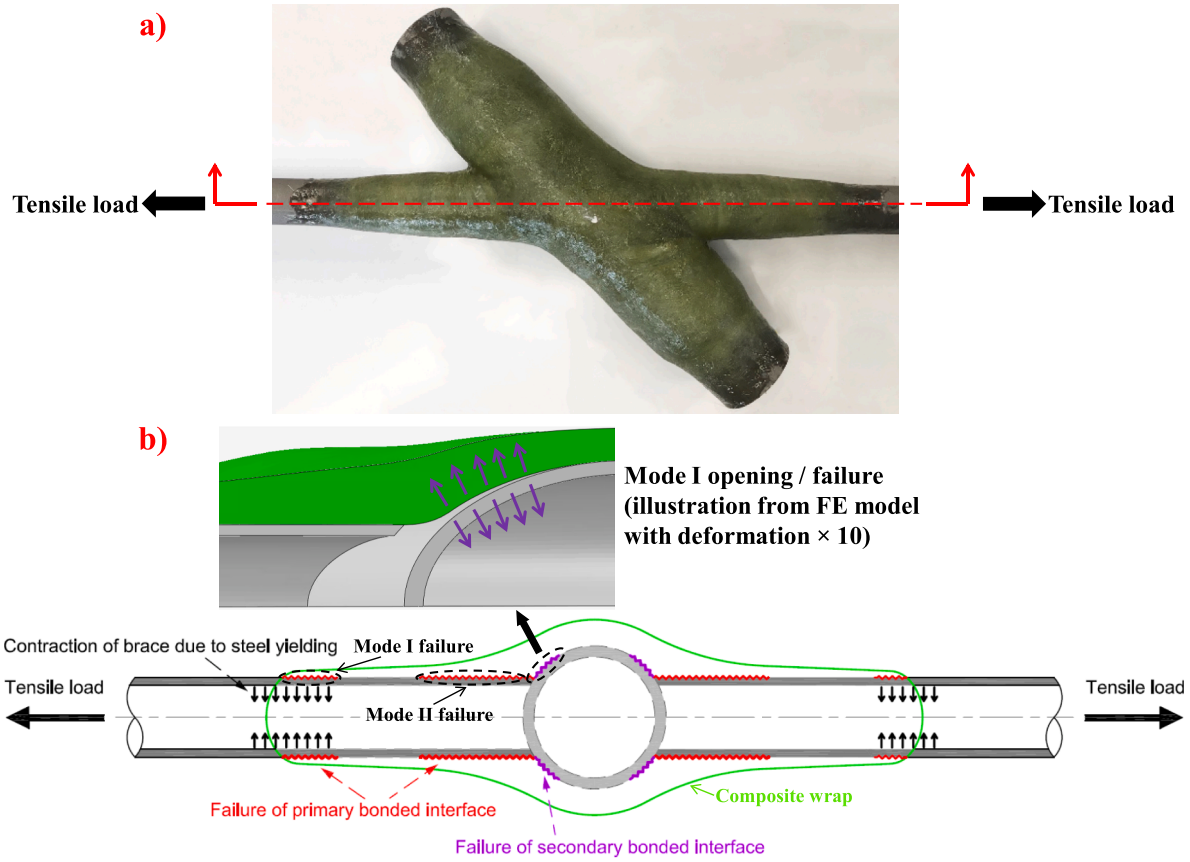

Fig. 1. Wrapped composite joints: a) the 45° small-scale X-joint specimen[3]; b) summary of failure modes and load transfer mechanism under tensile load[3].

2. Specimens and materials

The DCB tests are performed to characterize and quantify the mode I fracture behavior of the composite-steel bonded interface and the configuration of the DCB specimen is illustrated in Fig. 3. The steel is positioned as the upper adherend with thickness $h_{steel} = 3$ mm while the composite laminate is located as the lower adherend with thickness $h_{composite} = 7.62$ mm. The adherend length L and width B is 180 mm and 20 mm, respectively, and the pre-crack is inserted with length $a_0 = 60$ mm. The pre-crack length a_0 is defined as the distance between the section of the applied load and the pre-crack tip. The loading pin with length $L_p = 25$ mm is bonded to the upper and lower adherends for load transfer. The overview of the dimensions of the DCB specimens are summarized in Table 1. The DCB test is accomplished with 3 nominally identical specimens to characterize scattering of the material properties. The specimens are named as DCB-S1/2/3 where S refers to static test and 1/2/3 refers to specimen number 1, 2, 3, respectively.

The composite-steel bonded plate was manufactured and the test specimens were cut from the plate using water jet. The S355 mild steel plate was treated by grit blasting and degreased with acetone. A non-adhesive tape with 32 μm thickness was placed on the steel plate before lamination to create a pre-crack. Subsequently, the hand lay-up lamination was performed using E-glass fiber plies and a vinyl ester thermoset in a controlled factory environment at room temperature and humidity conditions with quality control to ensure good compaction and avoiding air gaps. The E-glass fiber plies are composed of bidirectional woven fabrics and chopped strand mat, and the composite laminate presents a fiber volumetric fraction ranging 30 %~32 %. The laminated plate was left for curing at a controlled environment of temperature and humidity and no post-curing was applied. It should be noted that the composite laminate was directly bonded on the steel plate without application of intermediate adhesive layer so that the thickness of the adhesive layer is negligible. Mechanical properties of the composite and steel adherends were measured by standard testing methods and are presented in Table 2.

3. Experiment and measurement set-up

The DCB test were conducted in the UTM 25 universal testing machine with a 15 kN load cell, as shown in Fig. 4. The specimen is connected to the fixture through the pin connection at the upper and lower adherend. The crack driving force is applied through the hydraulic jack to the upper adherend at a constant displacement rate of 1 mm/min. Prior to the test, the specimens were coated on the side to measure the full field displacements around the crack path using a 2-dimensional (2D) digital image correlation (DIC) system. A thin layer of white matt paint was coated to the side surface of the specimens followed by a sprayed black speckle pattern to create the measurement surface for DIC analysis. A camera with 21-megapixel resolution was set to take photos of the specimen at a frequency 1/3 Hz and a polarized blue light was use during the test to provide steady illumination conditions for accurate measurements. A block was placed on the specimen to provide a reference length for the DIC measurements, as shown in Fig. 5. After the test, the photos were imported into the GOM Correlate Pro software to track and measure the deformation of the specimens based on the surface component built at the reference stage, see Fig. 5.

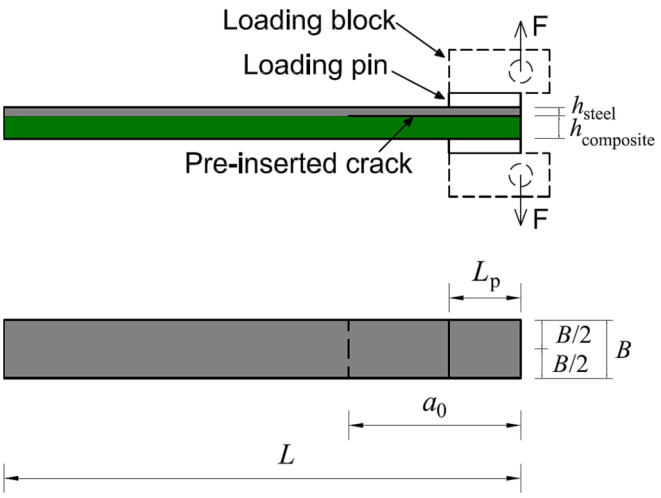

Fig. 3. Composite-steel DCB test specimen.

Table 1
Overview of DCB specimen dimensions (unit: mm).

Specimen	h_{steel}	$h_{composite}$	L	B	a_0	L_p
DCB-S1/2/3	3	7.62	180	20	60	25

Table 2
Mechanical properties of the steel and composite adherends.

Material	Mechanical properties	Average value (and CoV [%])	Standard
Steel	Tensile modulus – E	210000 N/mm^2 (5.74)	ISO 6892–1[40]
	Yield strength – σ_e	360.91 MPa (4.86)	
Composite	In-plane tensile modulus in x/y direction – $E_{x,t} = E_{y,t}$	11798 N/mm^2 (6.37)	ISO 527–1[41] and 527–2[42]
	In-plane tensile strength in x/y direction – $f_{x,t} = f_{y,t}$	216 MPa (5.78)	
	In-plane compressive modulus in x/y direction – $E_{x,c} = E_{y,c}$	12077 N/mm^2 (4.50)	ISO 14,126[43]
	In-plane compressive strength in x/y direction – $f_{x,c} = f_{y,c}$	200 MPa (3.79)	
	In-plane shear modulus – G_{xy}	3120 N/mm^2 (6.81)	ISO 14,129 [44]
	In-plane shear strength – $f_{xy,v}$	72.2 MPa (2.59)	

4. Finite element modeling (FEM)

The fracture behavior of DCB specimen was simulated by the 3D FE

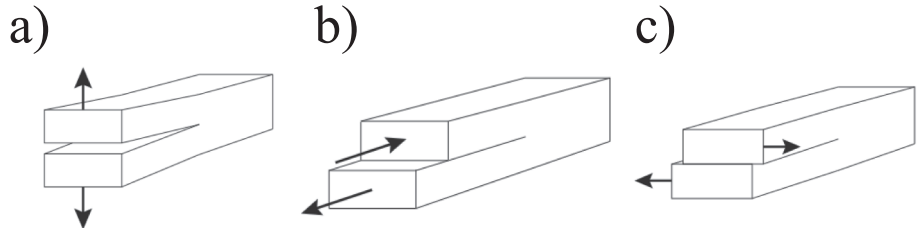

Fig. 2. Fracture modes of the interfacial cracking – a) mode I: opening; b) mode II: in-plane shear; c) mode III: out-of-plane shear.

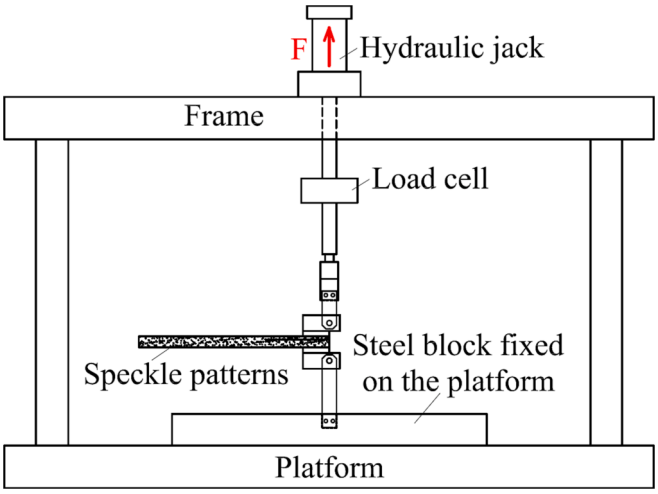

Fig. 4. The scheme of DCB test set-up.

model in ABAQUS in the quasi-static manner using the explicit solver [45] due to its advantages in computation convergence and dealing with non-linear behavior such as contact problems. Mass scaling method was conducted with definition of smooth step function to increase the computational efficiency. Fig. 6a) shows a representation of the boundary conditions applied in the DCB model. The symmetry boundary condition in global Z direction was applied to the back surface of the half model to save computational costs. The area of the steel and composite adherends glued with the loading pin designated as upper surface and lower surface was kinematically constrained (coupled) to the "Load" and the "Hold" reference point in all degrees of freedom, respectively. The crack driving force was applied through positive displacement in vertical translation (U2) to the reference point "Load" fixed in translation in global Z direction and rotation in global X and Y direction. The same degrees of freedom were fixed at the reference point "Hold" and the vertical translation U2 was also fixed to simulate the real constraints during the test.

The global mesh size is 2 mm according to the mesh sensitivity analysis in the joint modeling, which is not included in this paper. Linear element was used to save computational cost without sacrificing the simulation accuracy considering the relatively fine mesh size. The composite adherend was modelled using the 4-node tetrahedral solid element (C3D4), see Fig. 6b), attributed to its advantages in simulating stresses and strains in the through-thickness direction and in meshing composite laminate with curved and complex geometry. The steel adherend was meshed with 8-node hexahedral element (C3D8R) and 4 elements were meshed in the through-thickness direction to accurately simulate the bending-dominated deformation. The engineering constants were used to simulate elastic modulus of composite in the orthotropic direction using the material properties from experiments summarized in Table 2. In addition, the elastic modulus in through-thickness tensile and shear behavior is $E_3 = 5000$ N/mm^2 and $G_{13} = G_{23} = 2500$ N/mm^2, respectively. These values were obtained based on the manufacture data and calculation using classical laminate theory

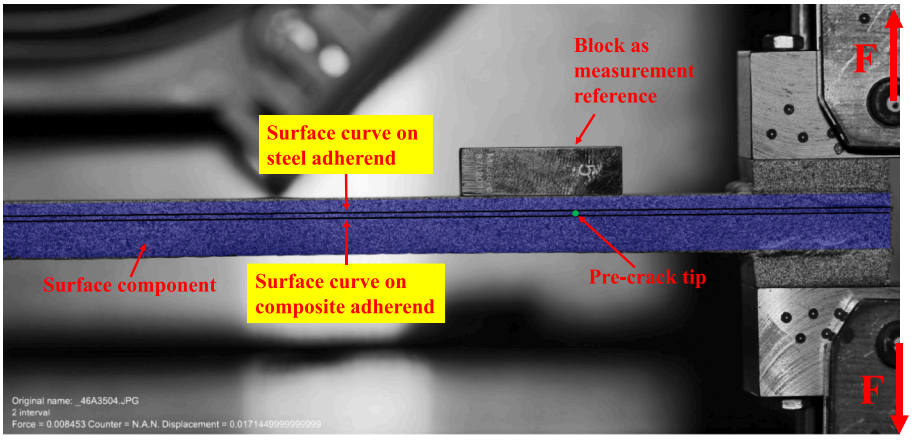

Fig. 5. DIC analysis in GOM Correlate Pro software.

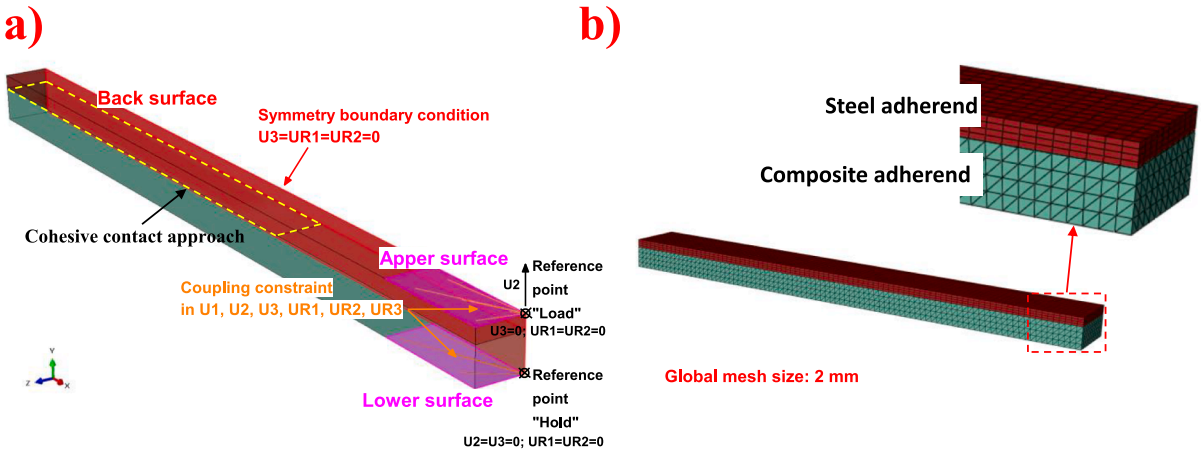

Fig. 6. DCB FE model: a) boundary conditions and cohesive contact definition; b) mesh overview.

and rule of mixture.

The cohesive contact approach was used to model the bonding of composite-steel interface as shown in Fig. 6a), which is primarily intended for situations where the adhesive layer thickness is negligible and is easier to define compared to cohesive elements. The cohesive zone model (CZM) was assigned to the contact surface pairs where the traction-separation law was introduced to describe the fracture behavior in between. Based on the experimental and numerical results of DCB specimens, a four-linear traction-separation law was proposed to replicate mode I fracture process of composite-steel bonded interface which will be explained thoroughly in section 4.

4.1. Mode I fracture process represented by a four-linear traction-separation law

Due to improved fracture toughness of resin, enhanced steel surface roughness and existence of fiber bridging, the fracture process of the composite-steel bonded interface does not follow the assumption of LEFM. On the contrary the non-linear FPZ is formed as shown in Fig. 7a) and the relation between the traction and the crack tip opening displacement (CTOD) of the pre-crack tip within the FPZ can be described by a four-linear cohesive law illustrated in Fig. 7b). Four critical stages are defined for further manipulation: "p" – onset of plasticity; "c" – onset of cracking; "b" – onset of fiber bridging; "f" – failure. Three distinct phenomena are described in the fracture process: 1) crack tip deformation, 2) softening and 3) fiber bridging. Two out of three phenomena, i.e., crack tip and fiber bridging, is consistent to the current literature [30,36,46,47]. The crack tip deformation is associated with small opening displacements and high traction values, whereas fiber bridging is associate with larger opening displacements and low tractions [46]. In addition, a transition phenomenon is proposed as softening where tractions reduce rapidly from σ_c to σ_b.

In the beginning of the fracture process the CTOD increases linearly until δ_p at stage "p" referring to onset of plasticity where the CTOD continues increasing under a constant traction value $\sigma_p = \sigma_c$ until stage "c" corresponding to onset of cracking. The short plateau between stage "p" and stage "c" is attributed to micro-fracture of the resin with the cavities of the steel surface roughness. It should be noted that in fracture of composite delamination, the existence of this plateau is absent, and stages "p" and "c" overlap with each other. The SERR dissipated to reach stage "c" (the orange area) is defined as the critical SERR for crack initiation or crack tip fracture resistance [36,46,47] with the symbol $G_{Ic,tip}$ while the distance between stage "p" and stage "c" is defined as the FPZ length for crack initiation designated as $FPZ_{Ic,tip}$. Subsequently, the tractions drop significantly until stage "b" due to the weak resistance of the resin inside the valley of the micro profile of steel surface against the pull-out force. The SERR dissipated from stage "c" to stage "b" is defined as the SERR due to softening (the green area) with the symbol of $G_{I,soft}$ while the distance between stage "c" and stage "b" is defined as the FPZ length due to softening designated as $FPZ_{I,soft}$. In the current literature, $G_{I,soft}$ and $FPZ_{I,soft}$ are considered as part of $G_{Ic,tip}$ and $FPZ_{Ic,tip}$, respectively [36,37], and the influence of considering or not considering them on values of $G_{Ic,tip}$ and $FPZ_{Ic,tip}$ is negligible in the mode I fracture process. However, the SERR due to softening is found to have significant contribution to the fracture resistance of the composite-steel bonded interface in mode II, which is not discussed in this study [48]. Therefore,

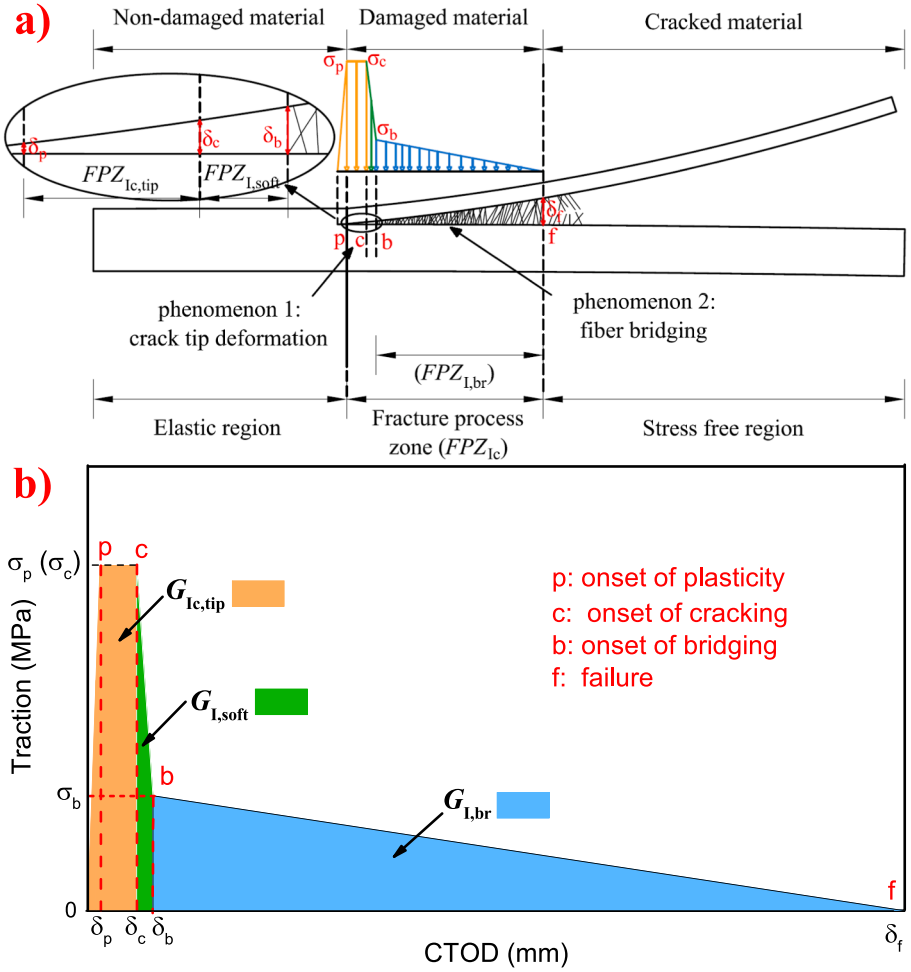

Fig. 7. Mode I fracture process of composite-steel bonded interface illustrated by a) schematic diagram and described by b) the four-linear traction-separation law.

$G_{I,soft}$ and $FPZ_{I,soft}$ are separately defined in the present nomenclature to have better control of variations of cohesive law shapes in different fracture modes. The softening is followed by fiber bridging where the traction values decrease gradually from σ_b at stage "b" to 0 at stage "f" as a consequence of the nesting of the chopped strand mat in the first ply of the composite laminate with the steel surface and with the adjacent woven fabrics. The SERR dissipated between stage "b" and stage "f" is defined as the SERR due to fiber bridging with the symbol of $G_{I,br}$ (the blue area). The distance between stage "b" and stage "f" is defined as the FPZ length due to fiber bridging designated as $FPZ_{I,br}$. When stage "f" is reached, the fracture surface is completely separated at the pre-crack tip and the SERR attains a constant value referred to as the critical SERR for crack propagation or steady state fracture resistance [37,46,47] designated as G_{Ic}. The distance between stage "p" and stage "f" is defined as the FPZ length for crack propagation designated as FPZ_{Ic}. It can be seen from Fig. 7 that

$$G_{Ic} = G_{Ic,tip} + G_{I,soft} + G_{I,br} \tag{1}$$

$$FPZ_{Ic} = FPZ_{Ic,tip} + FPZ_{I,soft} + FPZ_{I,br} \tag{2}$$

where $G_{I,br}$ and $FPZ_{I,br}$ are governing indicating that fiber bridging provides the majority of the fracture resistance to the bonded interface in mode I fracture process. In the presented research, the critical stages (stage "p", "c", "b" and "f") used in the defined four-linear cohesive law were determined through an approach that combines measurements of crack length a and CTOD through analysis of DIC data, along with SERR values calculated using EGM. More details in terms of this approach are given in Section 4. The values of the CTOD and traction at the critical stages, together with the critical SERR values ($G_{Ic,tip}$ and G_{Ic}), are summarized in Table 3.

5. Fracture data analysis

5.1. Determination of critical stages in the load–displacement response

The method to determine critical stages in the global response of DCB tests is explained in Fig. 8 where the load–displacement curve (in red) of the specimen DCB-S2 is compared to the variations of tangential stiffness in load–displacement response, crack length and CTOD with the applied displacement (in orange), respectively. It can be seen that stage "p", stage "c" and stage "f" refer to the turning points where decreasing rate of tangential stiffness grows suddenly and meanwhile increasing rate of crack length a and CTOD rises instantly. It should be noted that the part of the tangential stiffness curve exceeding 7-mm applied displacement is not presented in Fig. 8a) because big noise is introduced to the stiffness attributed to appearance of the inertia effect during the fiber bridging process. In this case, stage "f" refers directly to the peak load point on the load–displacement curve. Furthermore, stage "p" cannot be determined through observing the increasing rate of crack length a which starts to grow only after stage "c", but good agreement is reached between variation of tangential stiffness and CTOD to determine stage "p". Fig. 8b) indicates that measuring $FPZ_{Ic,tip}$ is difficult due to the limited crack extension and the summation of $FPZ_{Ic,tip}$ and $FPZ_{I,soft}$ is approximately 2.5 mm.

In FEM the critical stage "p" refers to the turning points where decreasing rate of tangential stiffness grows suddenly in the numerical load–displacement curve. Critical stages "c", "b" and "f" are determined when the corresponding contour colors of the output variable CSDMG (the scalar damage variable of the bonded interface) are observed at the pre-crack tip for the first time, as shown in Fig. 10. The contour color yellow, red and black refer to the damage valuable at critical stages "c" (0.875), "b" (0.995) and "f" (0.999), respectively, defined in the four-linear cohesive law.

5.2. Determination of crack length a and CTOD

In DCB test the crack length a and the CTOD were accurately measured by analysis of DIC measurement data in GOM Correlate Pro software. Two surface curves were built on the steel and composite adherends 0.5 mm parallel to the bonded interface (see Fig. 5) and the vertical displacement along them were read from surface component data. The present crack tip is determined as the location where the relative vertical displacement from the two surface curves starts to deviate, as shown in Fig. 9. The crack length a is the distance between the section of the applied load and the present crack tip while the CTOD is the subtraction of the vertical displacement from two surface curves at the pre-crack tip location.

In FEM the present crack tip is determined as the front of the yellow contour where the scalar damage variable of the bonded interface just reaches the input values (CSDMG = 0.875) corresponding to crack initiation, as shown in Fig. 10b) ~ d). The CTOD is obtained by subtracting the vertical displacement output in steel and composite adherend at the pre-crack tip, as shown in the enlargement side view in Fig. 10 a). Fig. 10 d), Fig. 10 c), and Fig. 10 b) illustrate the determination of the critical stages "c", "b" and "f" when the yellow, red, and black colors first appear on the contour plot of the pre-crack, corresponding to CSDMG values of 0.875, 0.995, and 0.999, respectively, defined in the four-linear cohesive law. It can also be observed in Fig. 10 that the longitudinal position of the present crack tip varies across the width of the specimen with a convex shape. This is due to the anticlastic bending of the specimen affected by both material properties (Poisson's ratio) and geometry of the specimens [46,47,49–51].

5.3. Determination of SERR

The strain energy release rate (SERR) was calculated using the extended global method (EGM) [26,27] where the total SERR is:

$$G_{total} = \frac{6}{B^2}\left[\frac{M_{steel}^2}{E_{steel}h_{steel}^3} + \frac{M_{composite}^2}{E_{composite}h_{composite}^3} - \frac{\left(M_{steel}+M_{composite}\right)^2}{E\left(h_{steel}+h_{composite}\right)^3}\right] \tag{3}$$

where E_{steel}, I_{steel}, $E_{composite}$, $I_{composite}$, E and I are the elastic modulus and the second moment of area in the *section* of the crack tip of the steel adherend, composite adherend and the specimen, respectively. B, h_{steel} and $h_{composite}$ are the width of the specimen, the height of steel and composite adherend, respectively, see Fig. 3. M_{steel} and $M_{compsosite}$ are the bending moments (assumed positive when counterclockwise) of the steel and composite adherend at the crack tip, respectively. The design of DCB specimens in this study did not satisfy the longitudinal strain based criterion [16], so the equivalent longitudinal strain ratio of the steel and composite adherends was introduced to guarantee pure mode I in mode partitioning of bi-material bonded joints [18]:

$$\beta = \frac{E_{composite}h_{composite}^2}{E_{steel}h_{steel}^2} \tag{4}$$

The applied moments can be resolved as:

Table 3
Input of parameters of the four-linear cohesive law used in modeling DCB test.

Critical stage	Onset of plasticity		Onset of cracking		Onset of fiber bridging		Failure		Critical SERR	
Symbols	δ_p (mm)	σ_p (MPa)	δ_c (mm)	σ_c (MPa)	δ_b (mm)	σ_b (MPa)	δ_f (mm)	σ_f (MPa)	$G_{Ic,tip}$ (N/mm)	G_{Ic} (N/mm)
Values	0.002	20	0.016	20	0.040	2	0.881	0	0.3	1.4

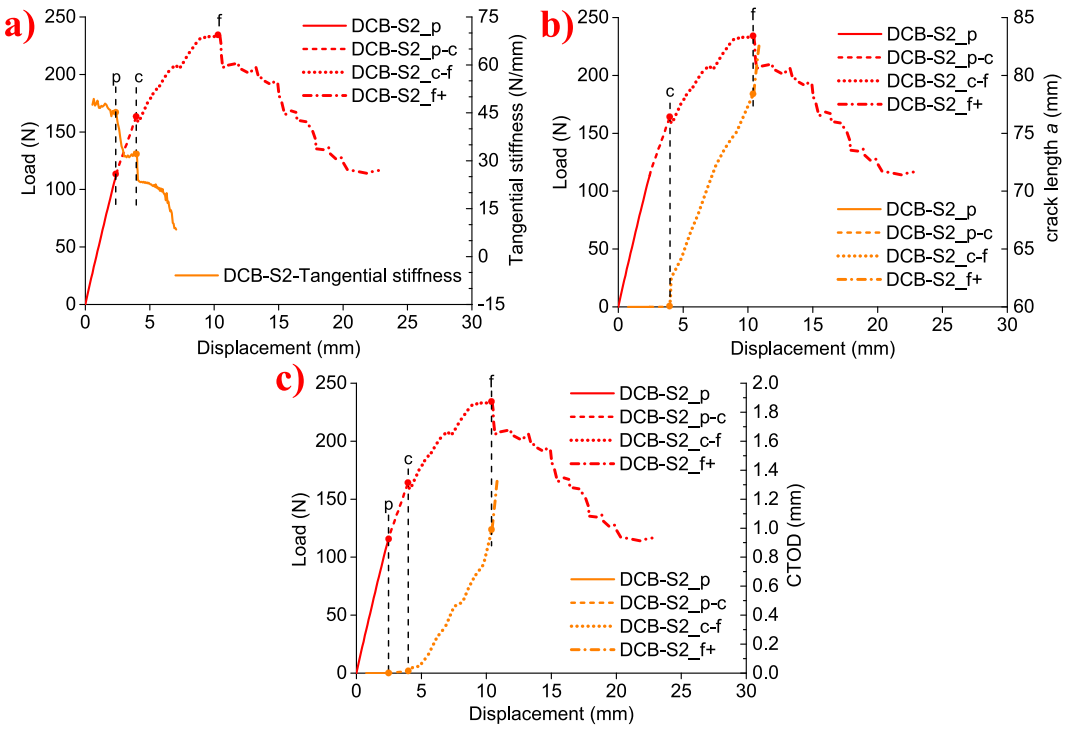

Fig. 8. Illustration of the method to determine critical stages of the load–displacement response in experiments through a) tangential stiffness, b) crack length a and c) CTOD – an example of specimen DCB-S2 (p, p-c, c-f, f + corresponds to elastic behavior until stage p, stage p to stage c, stage c to stage f, after stage f, respectively).

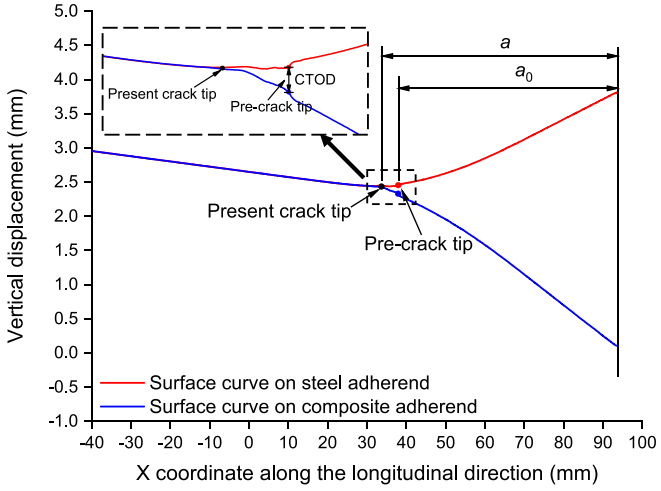

Fig. 9. Illustration of determination of a and CTOD in DIC.

$$M_{steel} = M_{\mathrm{I}} + M_{\mathrm{II}} \tag{5}$$

$$M_{composite} = -\beta M_{\mathrm{I}} + \psi M_{\mathrm{II}} \tag{6}$$

where ψ is defined as the bending stiffness ratio of steel and composite adherends to assure the identical curvature in the two adherends to obtain pure mode II:

$$\psi = \frac{E_{composite} I_{composite}}{E_{steel} I_{steel}} \tag{7}$$

Substitution of Equation (5) and Equation (6) into Equation (3) leads to the mode partition of G_{total} into G_{I} as:

$$G_{\mathrm{I}} = \frac{\left(\psi M_{steel} - M_{composite}\right)^2}{2B(\beta+\psi)^2}\left(\frac{1}{E_{steel} I_{steel}} + \frac{\beta^2}{E_{composite} I_{composite}} - \frac{(1-\beta)^2}{EI}\right) \tag{8}$$

In this study, $M_{steel} = Fa$, $M_{composite} = -Fa$. Therefore, the SERR in mode I can be calculated as:

$$G_{\mathrm{I}} = \frac{(\psi+1)^2 F^2 a^2}{2B(\beta+\psi)^2}\left(\frac{1}{E_{steel} I_{steel}} + \frac{\beta^2}{E_{composite} I_{composite}} - \frac{(1-\beta)^2}{EI}\right) \tag{9}$$

where the F is the applied load and a is the present crack length, respectively.

6. Results and discussion

6.1. DCB test results

The load–displacement curves of 3 specimens in DCB tests are shown in Fig. 12 where the critical stages are identified, and the associated values of applied displacement and load are summarized in Table 4. The fracture morphology is shown in Fig. 11. It can be seen from Fig. 12 that onset of plasticity (stage "p") corresponds to the elastic load limit at approximately 120 N followed by crack initiation at approximately 170 N (stage "c") where the load drops slightly due to softening. Subsequently, the existence of fiber bridging shown in Fig. 11a) leads to gradual increase of load until the peak load is reached at stage "f", where the FPZ for crack propagation is completely formed. It should be noted that stage "b" cannot be obtained from the tests due to the negligible fracture energy accumulated in the softening stage. Fig. 11b) and Fig. 11c) show the representative fracture morphology of the DCB specimens, and Fig. 11d) shows the height profile on the fracture surface of steel adherend. It can be seen that fiber bridging is really governing in mode I fracture process.

Fig. 13 and Fig. 14 present the crack length a and the CTOD measured during the DCB tests. It can be seen that the pre-crack tip opens at stage "p" but the CTOD is still limited (less than 0.02 mm) until crack initiates at stage "c". Subsequently, the crack length a and the CTOD develops progressively until stage "f" where these two variables increase at a constant rate. This indicates that FPZ for crack propagation is fully developed and crack starts to propagate in a stable manner.

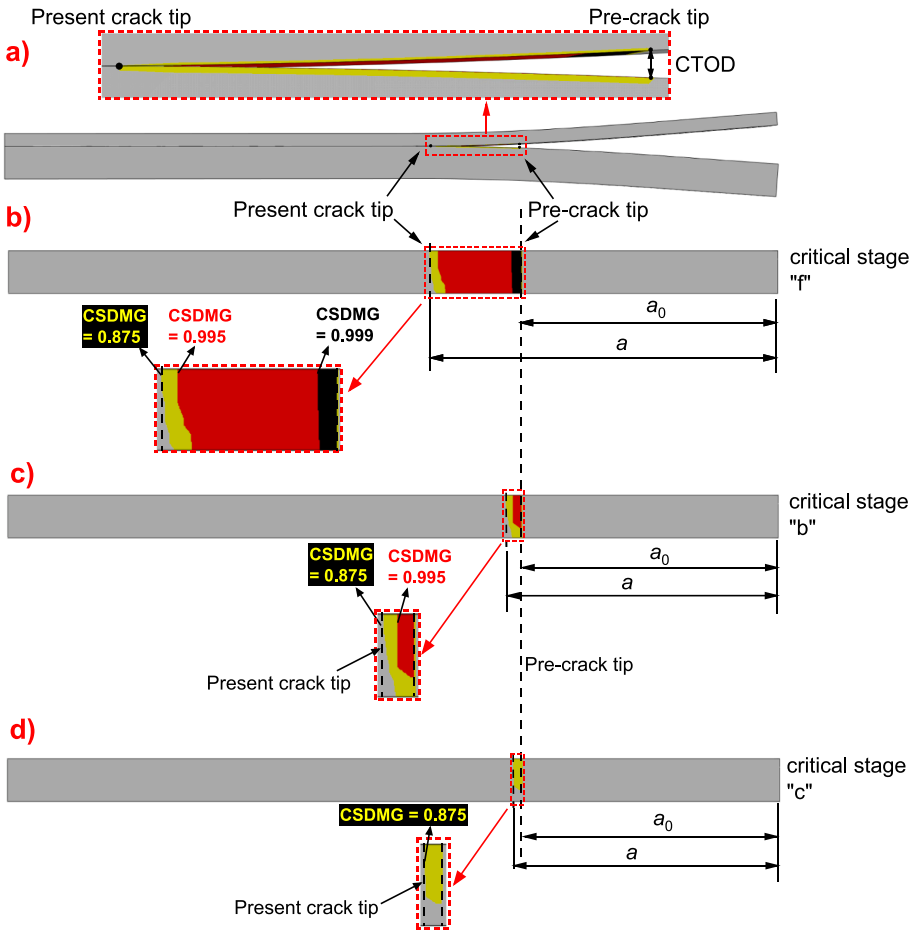

Fig. 10. Illustration of determination of critical stages, crack length a and CTOD in DCB FEM: a) the side view of DCB FE model at stage "f" and the enlargement view to determine CTOD; b) the plan view of the bonded interface on composite adherend identifying the present crack tip at stage "f"; c) the plan view at stage "b" identifying the present crack tip; d) the plan view at stage "c" identifying the present crack tip.

Table 4
Overview of displacement/load values at the critical stages of the fracture process in DCB test vs in DCB FEM.

Specimens or FE model	Onset of plasticity (stage "p")		Onset of cracking (stage "c")		Onset of bridging (stage "b")		Failure (stage "f")	
	Displacement (mm)	Load (N)	Displacement (mm)	Load (N)	Displacement (mm)	Load (N)	Displacement (mm)	Load (N)
DCB-S1	2.74	133.01	4.14	177.30	–	–	9.60	224.11
DCB-S2	2.42	113.60	3.98	164.37	–	–	10.45	233.62
DCB-S3	2.55	123.39	3.97	165.10	–	–	9.60	236.23
Average (and COV [%])	2.57 (5.11)	123.33 (6.43)	4.03 (1.93)	168.92 (3.51)	–	–	9.88 (4.05)	231.32 (2.25)
DCB-FEM	2.61	120.77	3.91	172.67	4.95	194.25	9.99	238.78
Deviation (%)	1.6	2.1	3.0	2.2	–	–	1.1	3.2

Based on the EGM, the mode I SERR of the composite-steel bonded interface was calculated and its relation with the crack extension Δa, i.e. the R-curve, is shown in Fig. 15. It can be seen that the critical SERR for crack initiation $G_{Ic,tip}$ is approximately 0.3 N/mm on average obtained at stage "c" and increases progressively during the fracture process to $G_{Ic} = 1.47$ N/mm on average at stage "f" defined as the critical SERR for crack propagation. The summation of the FPZ length due to softening $FPZ_{I,soft}$ and due to fiber bridging $FPZ_{I,br}$ refers to the distance of X co-ordinates between stage "c" and stage "f" on the R-curves while $FPZ_{Ic,tip}$ is neglected due to the its limited and unmeasurable values. The values of $G_{Ic,tip}$, G_{Ic} and $FPZ_{I,soft} + FPZ_{I,br}$ in 3 DCB specimens are summarized in Table 5. The average values of $FPZ_{I,soft} + FPZ_{I,br}$ in mode I fracture is approximately 16 mm.

6.2. Validation of DCB FEM

It can be seen in Fig. 12 that the numerical load–displacement curve (black curve) matches well with the testing curves in terms of elasticity, non-linear behavior, ultimate load and ductility. The values of load and applied displacement at critical stages are presented in Table 4 where the deviation of these variables compared to those in testing results are within 5 %. Therefore, it can be concluded that good match is reached in terms of global response in DCB modeling and DCB tests. Fig. 12 also shows that the load level in DCB numerical curve is larger than those in the experiments curves when the applied displacement value exceeds 15 mm. This is because in DCB tests the crack migrates from the first composite ply into the upper plies leading to reduction of the bending stiffness while in the FE model this crack migration is not simulated. The

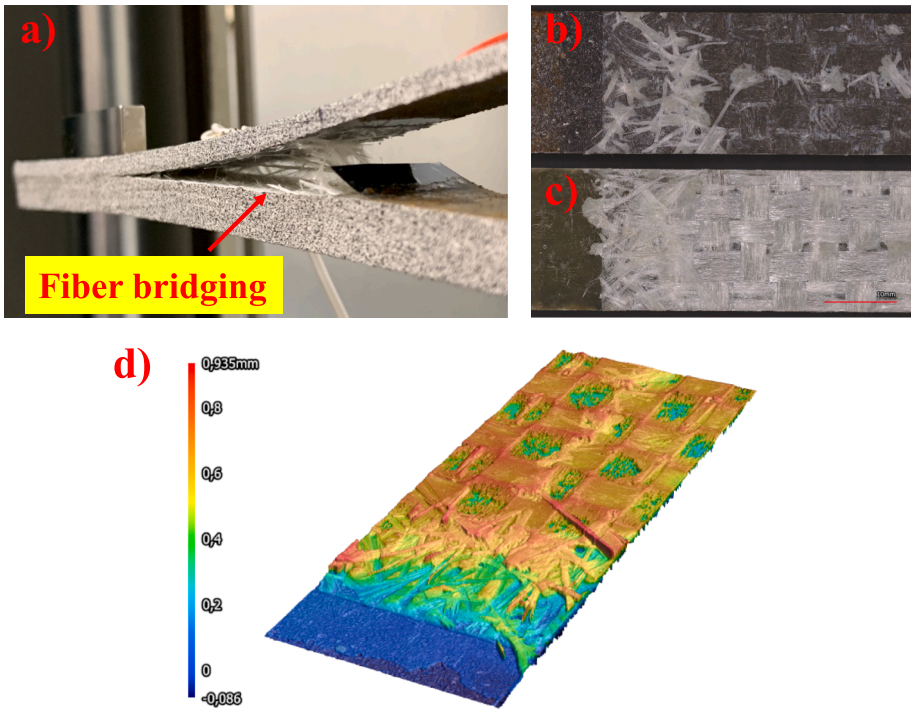

Fig. 11. Fracture surface morphology: a) fiber bridging observed during loading; b) fracture surface on steel and c) composite adherend; d) 3D scan of the fracture surface on the steel adherend.

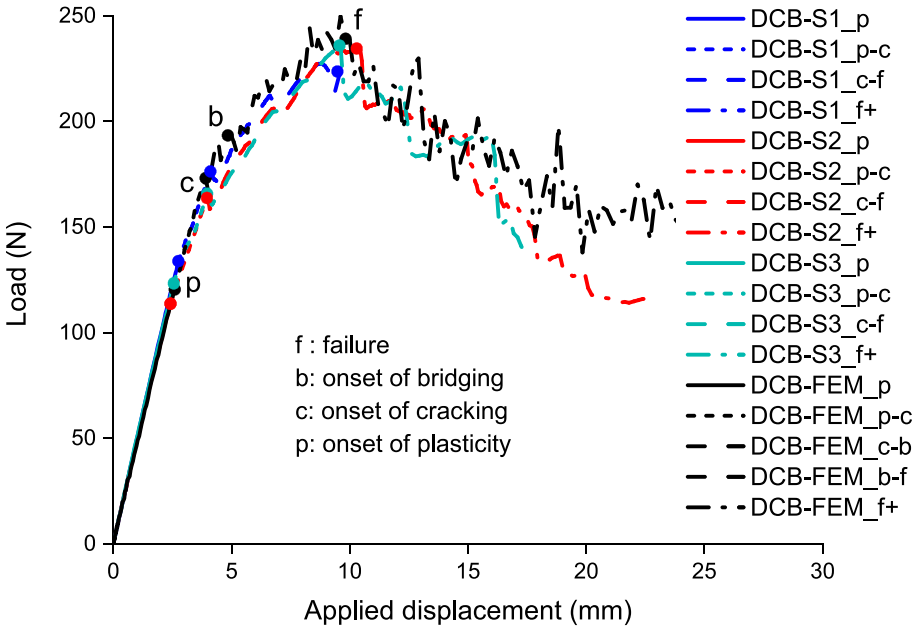

Fig. 12. Comparison of load–displacement response in DCB test vs modeling.

numerical load–displacement curve illustrates that stage "b" is reached after stage "c" through only 20 N load increase indicating the softening stage is momentary and the majority of the resistance after crack initiation comes from the fiber bridging until the peak load at stage "f".

In Fig. 13 and Fig. 14 the crack length a and the CTOD vs applied displacement obtained from the FE model are plotted for comparison with the testing curves. In both Figures good matches of the crack length and the CTOD in tests and in FEM are achieved. It can also be seen in Fig. 13 that the crack extension Δa between stage "c" and stage "f" obtained from FEM is approximately 16 mm which matches well to the average value from DCB tests. Therefore, it can be concluded that good matches of the failure process is achieved in DCB modeling vs DCB tests.

7. Conclusions

In the present research study, DCB experiments with help of FEM were used to explain and quantify mode I fracture behavior of glass fiber composite-steel bonded interface. Accurate measurements of the crack length a and the crack tip opening displacement (CTOD) were obtained during the test by analyzing digital image correlation (DIC) data while

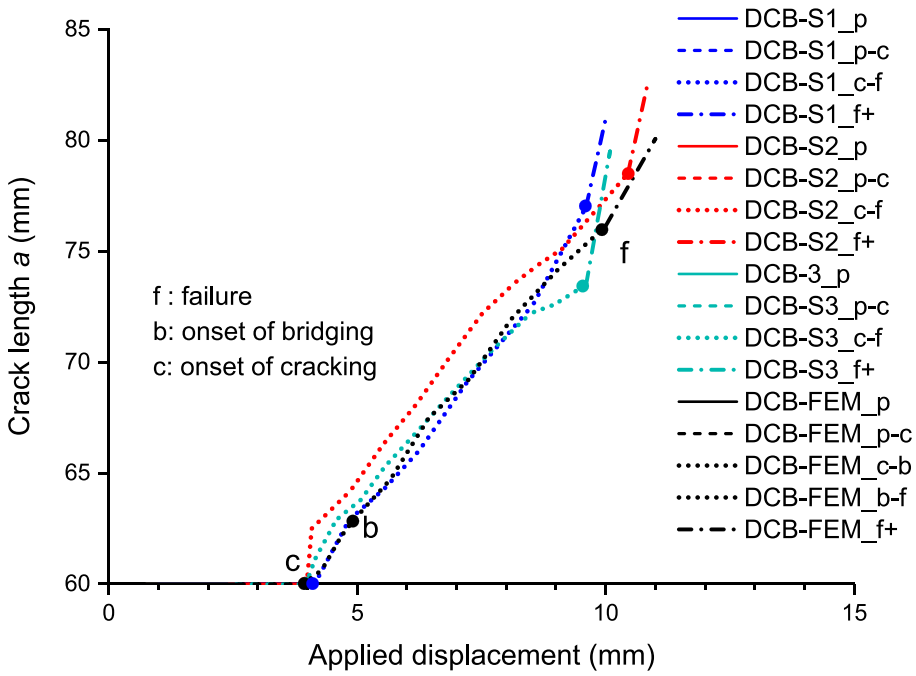

Fig. 13. Comparison of *a*-displacement relation in DCB test vs modeling.

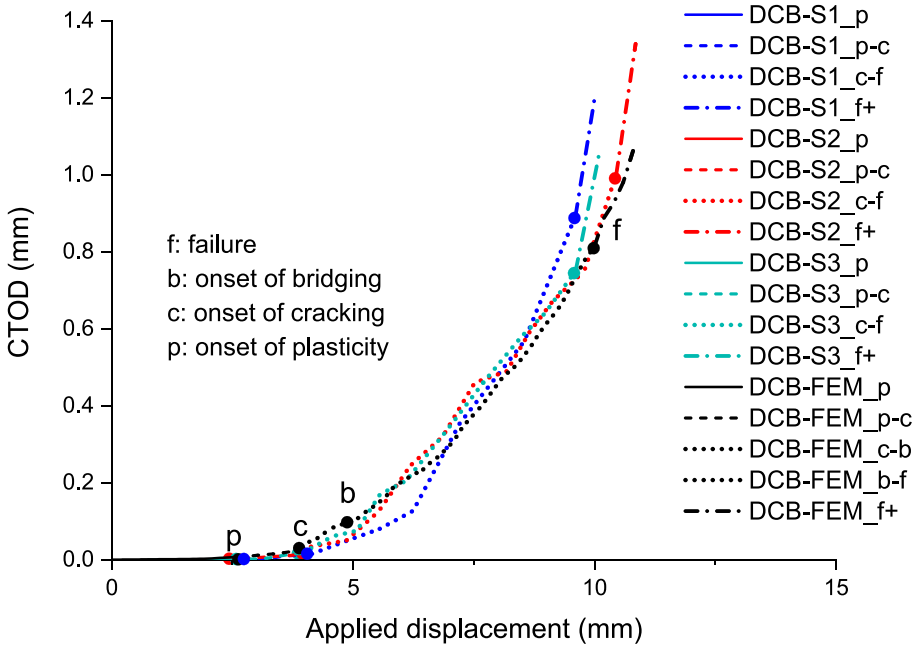

Fig. 14. Comparison of CTOD-displacement relation in DCB test vs modeling.

the strain energy release rate (SERR) was calculated using the extended global method (EGM). A four-linear cohesive law featuring onsets of plasticity, cracking and bridging and final failure was proposed and used in the DCB FE model to accurately simulate the mode I fracture behavior. Based on the experimental results and the numerical work, the following conclusion are drawn:

1. No adhesive (interfacial) failure was observed in the considered pure mode I fracture process. The fracture path is through the chopped strand mat of the first ply of the composite adherend (substrate failure) featuring significant fiber bridging behavior. The critical SERR $G_{Ic,tip}$ is 0.3 N/mm on average obtained for crack initiation while the critical SERR G_{Ic} is 1.47 N/mm on average obtained for crack propagation. The average FPZ length corresponding to summation of softening and fiber bridging is approximately 16 mm.
2. A four-linear traction-separation law is proposed to describe the mode I fracture process of composite-steel bonded interface. It describes three distinct phenomena: a) crack tip deformation, b) softening (newly proposed) and c) fiber bridging. Crack tip deformation is assumed to be attributed to the micro-cracking of resin within the valley of the micro profile of steel surface roughness. Softening refers to pull-out of resin in the steel surface cavities. Fiber bridging is the most governing fracture phenomenon as a consequence of the nesting of the chopped strand mat in the first laminate ply with the micro

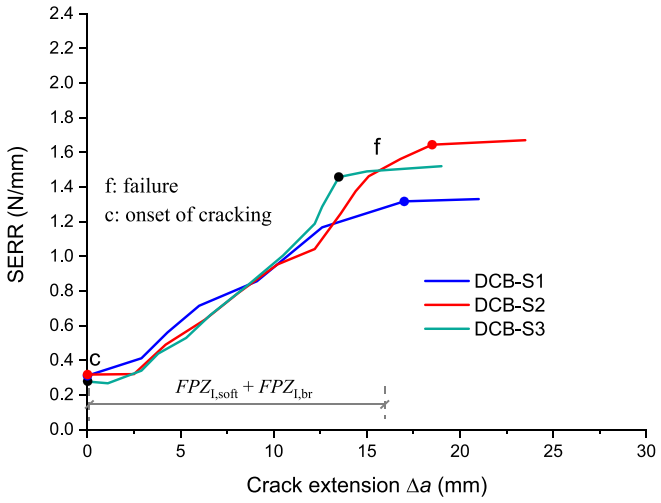

Fig. 15. R-curves of 3 specimens in DCB tests.

Table 5
Overview values of fracture resistance and FPZ length in DCB test.

Specimens	Critical SERR (N/mm)		$FPZ_{I,soft} + FPZ_{I,br}$ (mm)
	$G_{Ic,tip}$	G_{Ic}	
DCB-S1	0.31	1.32	17.0
DCB-S2	0.32	1.64	18.5
DCB-S3	0.28	1.46	13.5
Average (and COV[%])	0.30 (5.60)	1.47 (8.89)	16.3 (12.83)

profile of steel surface roughness and with the adjacent woven fabrics. These hypotheses should be validated through the micro-mechanical modeling which is not the scope of this research.

3. An approach is proposed to determine the critical stages of the four-linear cohesive law through the combination of detailed measurements of crack length and CTOD using 2D DIC, along with SERR values calculated by EGM.
4. The proposed four-linear cohesive law and the approach introduced to determine its critical stages were validated by good matches in both global (load–displacement response) and local behavior (crack length progression, CTOD development and FPZ length) between experiments and numerical simulation.

The presented characterization and understanding of the bi-material interface behavior goes beyond the first intended application in wrapped composite joints and are valuable for the wider field of engineering, such as aerospace, automotive and others.

CRediT authorship contribution statement

Pei He: Investigation, Data curation, Writing – original draft, Visualization, Formal analysis. **Marcio Moreira Arouche:** Writing – review & editing. **Mathieu Koetsier:** Data curation. **Marko Pavlovic:** Conceptualization, Methodology, Writing – review & editing, Supervision, Project administration, Funding acquisition.

Declaration of competing interest

The authors declare that they have no known competing financial interests or personal relationships that could have appeared to influence the work reported in this paper.

Data availability

Data will be made available on request.

Acknowledgement

This research is supported by NWO (Netherlands Organization for Scientific Research) under Demonstrator project “Fatigue resistant Wrapped FRP joints of structural hollow sections”, proj. no. 16949. The first author would also like to express his gratitude for the financial support from China Scholarship Council (CSC) under grant number of 201806260242. The authors are grateful for the acknowledge provision and fabrication of the wrapped composite joints by Tree Composites b. v., Versteden b.v.and Ask Romein b.v. The authors are very grateful for the assistance of technicians from Steven Lab II of TU Delft.

References

[1] M. Pavlovic M. Veljkovic P. Bogers “Method for making a virgin joint between two separate structural hollow sections and such a virgin joint” 11 542 708 2019 [Online]. Available: https://patents.google.com/patent/US11542708B2/en.
[2] He P, Pavlovic M. Feasibility of Wrapped FRP Circular Hollow Section Joints. In: in *Proceedings ofthe 17th International Symposiumon Tubular Structures*; 2019. p. 292–9. https://doi.org/10.3850/978-981-11-0745-0_043-cd.
[3] He P, Pavlovic M. Failure modes of bonded wrapped composite joints for steel circular hollow sections in ultimate load experiments. Eng Struct 2022;254(August 2021):113799. https://doi.org/10.1016/j.engstruct.2021.113799.
[4] He P, Feng W, Pavlovic M. Influence of steel yielding and resin toughness on debonding of wrapped composite joints. Compos Struct 2023;312(February): 116862. https://doi.org/10.1016/j.compstruct.2023.116862.
[5] Feng W, Pavlovic M. Fatigue behaviour of non-welded wrapped composite joints for steel hollow sections in axial load experiments. Eng Struct 2021;249(October): 113369. https://doi.org/10.1016/j.engstruct.2021.113369.
[6] Feng W, He P, Pavlovic M. “Combined DIC and FEA method for analysing debonding crack propagation in fatigue experiments on wrapped composite joints,”. Compos. Struct. 2022;297(March):115977. https://doi.org/10.1016/J.COMPSTRUCT.2022.115977.
[7] ASTM International, “ASTM D5528 - 13: 2014 - Standard Test Method for Mode I Interlaminar Fracture Toughness of Unidirectional Fiber-Reinforced Polymer Matrix Composites 1,” *West Conshohocken, PA ASTM Int.*, doi: 10.1520/D5528-13.
[8] International Standards Organization, “ISO 15024:2001 Fibre-reinforced plastic composites – Determination of mode I interlaminar fracture toughness, GIC, for unidirectionally reinforced material,” 2001. https://www.iso.org/standard/25581.html (accessed Jan. 20, 2023).
[9] Azari S, Ameli A, Papini M, Spelt JK. Analysis and design of adhesively bonded joints for fatigue and fracture loading: A fracture-mechanics approach. J Adhes Sci Technol 2013;27(15):1681–711. https://doi.org/10.1080/01694243.2012.748434.
[10] Ji G, Ouyang Z, Li G, Ibekwe S, Pang SS. Effects of adhesive thickness on global and local mode-I interfacial fracture of bonded joints. Int J Solids Struct 2010;47 (18–19):2445–58. https://doi.org/10.1016/j.ijsolstr.2010.05.006.
[11] Shokrieh MM, Heidari-Rarani M, Ayatollahi MR. Interlaminar fracture toughness of unidirectional DCB specimens: A novel theoretical approach. Polym Test 2012;31 (1):68–75. https://doi.org/10.1016/j.polymertesting.2011.08.012.
[12] Cabello M, Turon A, Zurbitu J, Renart J, Sarrado C, Martínez F. Progressive failure analysis of DCB bonded joints using a new elastic foundation coupled with a cohesive damage model. Eur J Mech A/Solids 2017;63:22–35. https://doi.org/10.1016/j.euromechsol.2016.12.004.
[13] Khoshravan M, Asgari Mehrabadi F. Fracture analysis in adhesive composite material/aluminum joints under mode-I loading; Experimental and numerical approaches. Int J Adhes Adhes 2012;39:8–14. https://doi.org/10.1016/j.ijadhadh.2012.06.005.
[14] Shimamoto K, Sekiguchi Y, Sato C. Effects of surface treatment on the critical energy release rates of welded joints between glass fiber reinforced polypropylene and a metal. Int J Adhes Adhes 2016;67:31–7. https://doi.org/10.1016/j.ijadhadh.2015.12.022.
[15] Shimamoto K, Sekiguchi Y, Sato C. The critical energy release rate of welded joints between fiber-reinforced thermoplastics and metals when thermal residual stress is considered. J Adhes 2016;92(4):306–18. https://doi.org/10.1080/00218464.2015.1031339.
[16] Wang W, Lopes Fernandes R, Teixeira De Freitas S, Zarouchas D, Benedictus R. How pure mode I can be obtained in bi-material bonded DCB joints: A longitudinal strain-based criterion. Compos Part B Eng 2018;153(July):137–48. https://doi.org/10.1016/j.compositesb.2018.07.033.
[17] Zambelis G, Da Silva Botelho T, Klinkova O, Tawfiq I, Lanouette C. Evaluation of the energy release rate in mode I of asymmetrical bonded composite/metal assembly. Eng Fract Mech 2018;190:175–85. https://doi.org/10.1016/j.engfracmech.2017.12.007.
[18] Arouche MM, Wang W, De Freitas ST. Strain-based methodology for mixed-mode I + II fracture : A new partitioning method for bi- material adhesively bonded joints. J Adhes 2019;95(5–7):385–404. https://doi.org/10.1080/00218464.2019.1565756.
[19] Wang W, De Freitas ST, Poulis JA, Zarouchas D. A review of experimental and theoretical fracture characterization of bi-material bonded joints. Compos Part B Eng 2020;206(October 2021):108537. https://doi.org/10.1016/j.compositesb.2020.108537.

[20] Lopes Fernandes R, Teixeira de Freitas S, Budzik MK, Poulis JA, Benedictus R. "Role of adherend material on the fracture of bi-material composite bonded joints,". Compos. Struct. 2020;252(May). https://doi.org/10.1016/j.compstruct.2020.112643.
[21] Ouyang Z, Ji G, Li G. "On approximately realizing and characterizing pure mode-I interface fracture between bonded dissimilar materials,". J. Appl. Mech. Trans. ASME 2011;78(3). https://doi.org/10.1115/1.4003366.
[22] Ouyang Z, Ji G, Li G, Ibekwe S, Pang S. A new idea of pure mode-I fracture test of bonded bi-materials. in *Proceedings of the ASME 2010 Pressure Vessels & Piping Division / K-PVP Conference*. 2010.
[23] de Moura MFSF, Campilho RDSG, Gonçalves JPM. Pure mode II fracture characterization of composite bonded joints. Int J Solids Struct 2009;46(6):1589–95. https://doi.org/10.1016/j.ijsolstr.2008.12.001.
[24] Shahverdi M, Vassilopoulos AP, Keller T. Mixed-Mode I/II fracture behavior of asymmetric adhesively-bonded pultruded composite joints. Eng Fract Mech 2014;115:43–59. https://doi.org/10.1016/j.engfracmech.2013.11.014.
[25] Williams JG. On the calculation of energy release rates for cracked laminates. Int J Fract 1988;36(2):101–19. https://doi.org/10.1007/BF00017790.
[26] De Morais AB, Pereira AB. Mixed mode I + II interlaminar fracture of glass / epoxy multidirectional laminates – Part 1: Analysis. Compos Sci Technol 2006;66:1889–95. https://doi.org/10.1016/j.compscitech.2006.04.006.
[27] Shahverdi M, Vassilopoulos AP, Keller T. Mixed-mode quasi-static failure criteria for adhesively-bonded pultruded GFRP joints. Compos Part A Appl Sci Manuf 2014;59:45–56. https://doi.org/10.1016/j.compositesa.2013.12.007.
[28] Chauffaille S, Jumel J, Shanahan MER. Elasto-plastic analysis of the single cantilever beam adhesion test. Eng Fract Mech 2011;78(13):2493–504. https://doi.org/10.1016/j.engfracmech.2011.06.009.
[29] Saleh MN, Budzik MK, Saeedifar M, Zarouchas D, Teixeira De Freitas S. On the influence of the adhesive and the adherend ductility on mode I fracture characterization of thick adhesively-bonded joints. Int J Adhes Adhes 2021;115(September 2022):103123. https://doi.org/10.1016/j.ijadhadh.2022.103123.
[30] Heide-Jørgensen S, Teixeira de Freitas S, Budzik MK. On the fracture behaviour of CFRP bonded joints under mode I loading: Effect of supporting carrier and interface contamination. Compos Sci Technol 2018;160:97–110. https://doi.org/10.1016/j.compscitech.2018.03.024.
[31] Hu P, Pulungan D, Tao R, Lubineau G. Influence of curing processes on the development of fiber bridging during delamination in composite laminates. Compos Part A Appl Sci Manuf 2021;149(March):106564. https://doi.org/10.1016/j.compositesa.2021.106564.
[32] Hu P, Pulungan D, Lubineau G. An enriched cohesive law using plane-part of interfacial strains to model intra/inter laminar coupling in laminated composites. Compos Sci Technol 2020;200(May):108460. https://doi.org/10.1016/j.compscitech.2020.108460.
[33] Elices M, Guinea GV, Gómez J, Planas J. The cohesive zone model: Advantages, limitations and challenges. Eng Fract Mech 2001;69(2):137–63. https://doi.org/10.1016/S0013-7944(01)00083-2.
[34] Papanastasiou P, Sarris E. Cohesive zone models. Elsevier Ltd 2017. https://doi.org/10.1016/B978-0-08-100781-5.00006-3.
[35] Shahverdi M, Vassilopoulos AP, Keller T. Mixed-Mode I/II fracture behavior of asymmetric composite joints. Procedia Struct Integr 2016;2:1886–93. https://doi.org/10.1016/j.prostr.2016.06.237.
[36] Cameselle-Molares A, Vassilopoulos AP, Renart J, Turon A, Keller T. Numerical simulation of two-dimensional in-plane crack propagation in FRP laminates. Compos Struct 2018;200(April):396–407. https://doi.org/10.1016/j.compstruct.2018.05.136.
[37] Heidari-Rarani M, Shokrieh MM, Camanho PP. Finite element modeling of mode i delamination growth in laminated DCB specimens with R-curve effects. Compos Part B Eng 2013;45(1):897–903. https://doi.org/10.1016/j.compositesb.2012.09.051.
[38] Shokrieh MM, Heidari-Rarani M, Ayatollahi MR. Delamination R-curve as a material property of unidirectional glass/epoxy composites. Mater Des 2012;34:211–8. https://doi.org/10.1016/j.matdes.2011.08.006.
[39] Martinelli E, Hosseini A, Ghafoori E, Motavalli M. "Behavior of prestressed CFRP plates bonded to steel substrate: Numerical modeling and experimental validation,". Compos. Struct. 2019;207(August 2018):974–84. https://doi.org/10.1016/j.compstruct.2018.09.023.
[40] International Standards Organization, "ISO 6892-1 International Standard INTERNATIONAL STANDARD ISO 6892-1:2009(E) Metallic materials — Tensile testing — Part 1: Method of test at room temperature 1," *Met. Mater.*, vol. 2009, p. 64, 2009.
[41] International Standards Organization, "ISO 527-1:2012 - Plastics - Determination of tensile properties - Part 1: General principles," 2012, [Online]. Available: www.iso.org.
[42] International Standards Organization, "ISO 527-2:1996 – Plastics — Determination of tensile properties – Part 2: Test conditions for moulding and extursion plastics," 2009, [Online]. Available: http://www.chemshow.cn/UploadFile/datum/1000/huayangyq2008w_2009420145250792688.pdf.
[43] International Standards Organization, "ISO 14126:1999 - Fibre-reinforced plastic composites - Determination of compressive properties in the in-plane direction," 1999.
[44] International Standards Organization, "ISO 14129: 1997 Fibre-reinforced plastic composites — Determination of the in-plane shear stress/shear strain response, including the in-plane shear modulus and strength, by the plus or minus 45 degree tension test method," 1997.
[45] D.S.S. Corp. "ABAQUS/Explicit User's Manual," 2019.
[46] Joki RK, Grytten F, Hayman B, Sørensen BF. "A mixed mode cohesive model for FRP laminates incorporating large scale bridging behaviour,". Eng. Fract. Mech. 2020;239(September 2019):107274. https://doi.org/10.1016/j.engfracmech.2020.107274.
[47] Joki RK, Grytten F, Hayman B, Sørensen BF. Determination of a cohesive law for delamination modelling - Accounting for variation in crack opening and stress state across the test specimen width. Compos Sci Technol 2016;128:49–57. https://doi.org/10.1016/j.compscitech.2016.01.026.
[48] Pei He MP, Koetsier M, Mylonopoulos V. Mode II fracture behavior of glass fiber composite-steel bonded interface – experiments and CZM. Compos part B Eng (under Rev 2023.
[49] Kotousov A, Lazzarin P, Berto F, Harding S. Effect of the thickness on elastic deformation and quasi-brittle fracture of plate components. Eng Fract Mech 2010;77(11):1665–81. https://doi.org/10.1016/j.engfracmech.2010.04.008.
[50] Jiang Z, Wan S, Keller T, Fang Z, Vassilopoulos AP. Influence of curved delamination front on R-curve of DCB specimen. Compos Struct 2019;227(June):111311. https://doi.org/10.1016/j.compstruct.2019.111311.
[51] Davidson BD. An analytical investigation of delamination front curvature in double cantilever beam specimens. J Compos Mater 1990;24(11):1124–37. https://doi.org/10.1177/002199839002401101.